Efficient enhancement of turbulent entrainment by small-scale shear instability

Tomoaki Watanabe[1,2] †

[1]Department of Mechanical Engineering and Science, Kyoto University, Kyoto 615-8540, Japan

[2]Education and Research Center for Flight Engineering, Nagoya University, Furo-cho, Chikusa, Nagoya 464-8603, Japan

(Received xx; revised xx; accepted xx)

Turbulent entrainment is a process by which a locally turbulent region draws in an outer irrotational fluid. A large number of small-scale vortices and shear layers exist near the turbulent/non-turbulent interface; these features influence the local entrainment process. Direct numerical simulations of a turbulent front evolving into a quiescent flow without mean shear show that the entrainment rate is amplified by triggering the instability of small-scale shear layers via weak perturbations with a wavelength matching that of the unstable mode of the shear layers. Imposing artificial perturbations with a length scale of approximately 30 times the Kolmogorov scale leads to the rapid collapse of small-scale shear layers due to instability, generating vortices near the turbulent/non-turbulent interface. Amplification of the entrainment rate is linked to the enlarged area and increased propagation velocity of the interface. The impact of perturbations on the entrainment rate becomes most pronounced when the flow evolves over approximately 7 times the Kolmogorov time scale, after which their influence diminishes over time. Additionally, the increase in entrainment rate is dictated by the ratio of the perturbation amplitude to the Kolmogorov velocity scale. The entrainment enhancement process is governed by Kolmogorov scales, suggesting that even weak perturbations can amplify the entrainment rate in high Reynolds number flows.

1. Introduction

Turbulent entrainment is the process by which a localised turbulent region draws in an outer non-turbulent (irrotational) fluid, leading to the expansion of the turbulent region. Entrainment plays a crucial role in various flows encountered in engineering and physics and is also evident in many environmental flows, such as atmospheric boundary layers (Schols 1984; Mahrt 1999) and clouds (Mellado 2017). At a cloud edge, dry air from an external region is often mixed into the cloud (Sardina *et al.* 2015). Entrainment significantly influences turbulent transport processes, especially in scalar mixing (e.g. heat and substances) (Westerweel *et al.*

† Email address for correspondence: watanabe.tomoaki.8x@kyoto-u.ac.jp

2009). Consequently, the control and enhancement of turbulent entrainment remain important topics in both science and engineering (da Silva *et al.* 2014).

Over the past decades, extensive research has been conducted to understand the entrainment process, emphasising the turbulent/non-turbulent interface (TNTI) layer that separates turbulent from non-turbulent regions (Westerweel *et al.* 2005; Holzner & Lüthi 2011; Taveira *et al.* 2013; van Reeuwijk & Holzner 2014; Krug *et al.* 2015; Jahanbakhshi & Madnia 2016; Watanabe *et al.* 2016*b*), as summarised in da Silva *et al.* (2014). The TNTI layer appears in canonical turbulent flows, such as jets, wakes and mixing layers. The local entrainment process in many such flows is dominated by small-scale turbulent motions located at or near the TNTI layer. Larger-scale motions predominantly dictate the total entrainment rate by influencing the area of the interface (Mistry *et al.* 2016; Krug *et al.* 2017). Notably, the TNTI layer forms near small-scale vortices (vortex tubes) and shear layers (da Silva *et al.* 2011; Elsinga & da Silva 2019; Neamtu-Halic *et al.* 2021; Hayashi *et al.* 2021*b*). Shear layers, originally termed vortex sheets due to their inherent vorticity, are sheetlike structures exhibiting shearing motion (Vincent & Meneguzzi 1994). Recent studies use the term shear layers to emphasise that their essential characteristic is shear rather than vorticity (Eisma *et al.* 2015; Watanabe *et al.* 2020*b*; Gul *et al.* 2020; Fiscaletti *et al.* 2021). This study employs "shear layers" to denote small-scale shear layers arising from velocity fluctuations, distinguishing them from those resulting from the mean velocity gradient, the latter being large-scale structures. The properties of the small-scale vortices and shear layers provide reasonable explanations for the entrainment process described by fluid particle movements and vorticity transport near the TNTI layer (Taveira & da Silva 2014; Jahanbakhshi *et al.* 2015; Watanabe *et al.* 2017; Elsinga & da Silva 2019; Hayashi *et al.* 2021*b*; Neamtu-Halic *et al.* 2021). These studies infer that vortices and shear layers within the TNTI layer play dominant roles in the entrainment process.

Compared to vortices, small-scale shear layers have received limited investigation due to challenges in their identification. Recent advancements in identifying shear layers based on novel mathematical treatments of velocity gradient tensors have enabled researchers to scrutinise their characteristics, as summarised herein (Kolář & Šístek 2014). The shear layer is one of the smallest turbulent structures, characterised using the Kolmogorov scales, and exhibits biaxial straining motion (Elsinga & Marusic 2010; Watanabe *et al.* 2020*b*; Fiscaletti *et al.* 2021). The interplay between shear and biaxial strain leads to substantial enstrophy production and self-amplification of strain. Moreover, the velocity field induced by shear layers makes a more pronounced contribution to the energy cascade compared to that induced by vortex tubes (Enoki *et al.* 2023). The stability of small-scale shear layers has also been investigated, given their role in vortex formation in turbulent regions. Prior to the investigation of small-scale shear layers, parallel shear flows had been theoretically studied as approximations of large-scale shear layers induced by a mean flow. The flow is inherently unstable against weak perturbations, leading to layer roll-up due to the Kelvin–Helmholtz instability. Linear stability theory suggests that parallel shear flows are most unstable in the presence of perturbations with a specific wavelength (Betchov & Szewczyk 1963). Similarly, small-scale shear layers in turbulence generate vortices in a process reminiscent of the Kelvin–Helmholtz instability (Vincent & Meneguzzi 1994; Watanabe *et al.* 2020*b*). Recent studies of small-scale shear layers confirmed the optimal wavelength for the small-scale shear instability, which is approximately 30 times the Kolmogorov scale η (Watanabe & Nagata 2023). When turbulence is subject to perturbations of this wavelength, the shear layers promptly collapse, resulting in a higher population of vortices arising from the shear instability. The evolution of shear layers is largely unaffected by perturbations with wavelengths much larger or smaller than 30η. The optimal perturbation wavelength of 30η was determined using

two simulations (Watanabe & Nagata 2023). One is a direct numerical simulation (DNS) of turbulent flows, which examines the length and velocity scales of the shear layers. The other is a numerical simulation of a modelled shear layer based on a conditionally averaged flow field observed around the shear layers in DNS. The first has confirmed that shear layers have a typical thickness δ of 4η regardless of Reynolds numbers. Simulating modelled shear layers suggests that the optimal wavelength for shear instability is 7δ, which is consistent with the stability analysis of uniform shear layers (Lin & Corcos 1984). Because of the probability distribution of δ, perturbations with a wavelength of approximately 30η effectively promote the instability of many shear layers.

Previous studies concerning the entrainment process and small-scale shear instability suggest the potential for enhancing entrainment by modulating small-scale shear layers. Given the efficacy of flow control strategies that exploit various flow instabilities to amplify the effects of weak disturbances (Cattafesta III & Sheplak 2011), it is plausible that manipulating small-scale shear layers can similarly lead to efficient flow control. In this study, numerical experiments are carried out to explore entrainment enhancement by stimulating small-scale shear layers, employing the DNS of a turbulent front perturbed by artificial velocity fluctuations with a wavelength comparable to the unstable mode of shear layers.

2. DNS of a turbulent front evolving into a non-turbulent fluid

DNS is conducted for a turbulent front evolving into a non-turbulent fluid without mean shear. The flow configuration aligns with previous works (Cimarelli *et al.* 2015; Silva *et al.* 2018; Watanabe *et al.* 2020*a*), which are briefly outlined herein. The governing equations are the incompressible Navier–Stokes equations, which are solved using an in-house finite-difference code based on the fractional step method (Watanabe *et al.* 2020*b*). The code employs a fourth-order fully conservative central difference and third-order Runge–Kutta schemes for spatial and temporal discretisation (Morinishi *et al.* 1998). The initial field is generated by embedding homogeneous isotropic turbulence (HIT) within a quiescent fluid. Snapshots from DNS databases of statistically steady HIT (Watanabe *et al.* 2020*b*) are used. The computational domain is set as a cube with a side length L. Periodic boundary conditions are applied in three directions. Within the coordinate system (x, y, z), $y = 0$ is positioned at the domain centre and $(x, z) = (0, 0)$ is anchored at the corner of the x–z plane. During the initialisation phase, the velocity field u_i of HIT is modified by the top-hat function $C(y)$:

$$C(y) = 0.5 + 0.5\tanh\left[\frac{4}{\Delta_I}\left(1 - \frac{2|y - L/2|}{L_T}\right)\right], \tag{2.1}$$

resulting in $C(y)u_i(x, y, z)$, with $L_T = L/3$ and $\Delta_I = 10\eta$, where η is the Kolmogorov scale of HIT. Turbulence, centred at $y = 0$ with an initial width of L_T, evolves into the surrounding non-turbulent fluid. By definition, $C = 1$ in the turbulent region and $C = 0$ in the non-turbulent region. Figure 1 shows a two-dimensional profile of vorticity magnitude $\omega = |\nabla \times \boldsymbol{u}|$ after the evolution of turbulence from its initial state. The turbulent region exhibits large values of ω, and grows by entraining non-turbulent fluid.

The flow is statistically homogeneous in the x and y directions. Averages of flow variables, represented by $\overline{f}$, are determined as spatial averages over the x–z planes as functions of y and time t. A fluctuating component of a variable f is expressed as $f' = f - \overline{f}$. The turbulent Reynolds number is given by $Re_\lambda = u_{rms}\lambda/\nu$. Here, ν is the kinematic viscosity, $u_{rms} = \sqrt{\overline{u_i'u_i'/3}}$ is the root-mean-square (rms) of velocity fluctuations, and $\lambda = \sqrt{15\nu u_{rms}^2/\varepsilon}$ is the Taylor microscale. Throughout this paper, successive indices imply summation. The average kinetic energy dissipation rate is $\varepsilon = \overline{2\nu S_{ij}S_{ij}}$, and the rate-of-strain tensor is

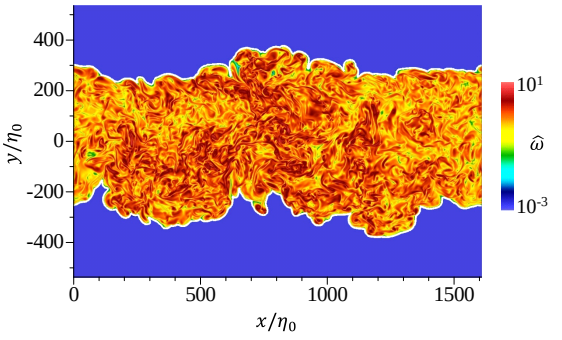

Figure 1: Distribution of vorticity magnitude ω in a turbulent front at $t = 14\tau_{\eta 0}$ for R4. The white lines represent the irrotational boundary. The normalised vorticity magnitude $\hat{\omega}$ is defined as ω divided by the mean value at $y = 0$.

$S_{ij} = (\partial u_i/\partial x_j + \partial u_j/\partial x_i)/2$. The Kolmogorov length, time and velocity scales are defined as follows: $\eta = (\nu^3/\varepsilon)^{1/4}$, $\tau_\eta = (\nu/\varepsilon)^{1/2}$ and $u_\eta = (\nu\varepsilon)^{1/4}$, respectively. Hereafter, a subscript 0 indicates statistics at $y = 0$ of the initial condition without perturbations, such as η_0 and $u_{\eta 0}$.

The evolution of the turbulent front is analysed under two distinct initial conditions. In the first case, the velocity field of HIT, denoted as $\boldsymbol{u}_{HIT}$, serves as the initial field, i.e. $\boldsymbol{u} = C\boldsymbol{u}_{HIT}$. In the second case, solenoidal velocity perturbations $\boldsymbol{u}_P$ are introduced to the velocity field in the turbulent region. The perturbed velocity field is formulated as $\boldsymbol{u} = C(\boldsymbol{u}_{HIT} + \boldsymbol{u}_P)$. A prior study addressed the impacts of $\boldsymbol{u}_P$ on small-scale shear instability in HIT, where the changes due to the promoted instability were discussed in terms of the number of vortices, energy dissipation, enstrophy production and strain self-amplification (Watanabe & Nagata 2023). Adopting this same methodology, $\boldsymbol{u}_P$ is described using sinusoidal functions: $\boldsymbol{u}_P = \left[u_f \sin(2\pi y/\lambda_f), u_f \sin(2\pi z/\lambda_f), u_f \sin(2\pi x/\lambda_f)\right]$, where u_f is the amplitude and λ_f is the wavelength. Different perturbation forms, such as random disturbances with a single length scale, were tested for HIT (Watanabe & Nagata 2023), showing that the evolution of perturbed HIT remains independent of perturbation type.

The parameters for DNS are detailed as follows. Five DNS databases of HIT with $Re_\lambda = 43$, 72, 128, 202 and 296 are labelled as R1, R2, R3, R4 and R5, respectively. The numbers of grid points N^3 for these cases are: 256^3, 512^3, 1024^3, 2048^3 and 4096^3, ensuring a grid spacing smaller than 0.8η. Cases without perturbations, i.e. $\boldsymbol{u}_P = (0, 0, 0)$, are simply designated as R1 through R5. Cases incorporating perturbations are designated as R$n\Lambda a$ with $n = 1, ..., 5$, indicating the Reynolds number, where Λ = S or L distinguishes the wavelength λ_f and $a = u_f/u_{\eta 0}$ is the normalised amplitude. The designation Λ = S corresponds to a perturbation of $\lambda_f = 30\eta_0$, namely the optimal wavelength of small-scale shear instability (Watanabe & Nagata 2023), whereas Λ = L assumes a larger wavelength, $\lambda_f = 140\eta_0$. The normalised amplitude a ranges between 1.0 and 2.6. For instance, R2S14 considers turbulence at $Re_\lambda = 72$ with a perturbation defined by $\lambda_f = 30\eta_0$ and $u_f/u_{\eta 0} = 1.4$. Most simulations adapt perturbations with $\lambda_f = 30\eta_0$ (Λ = S). One additional case for R2 with Λ = L ($\lambda_f = 140\eta_0$), in which the perturbation is unlikely to influence the evolution of small-scale shear layers (Watanabe & Nagata 2023), is designated as R2L14. Each simulation is allowed to progress until $t = 15\tau_{\eta 0}$. 3D data files for post-processes are saved at intervals close to $\tau_{\eta 0}$. Ensemble averages are obtained from N_S simulations, each initialised with different snapshots of HIT. The values of N_S are 10, 5, 3, 1 and 1, applied sequentially from cases R1 to R5. The perturbations are introduced to the initial velocity field of shear-free

turbulent fronts. Appendix A examines the dependence of the flow evolution on the time at which perturbations are introduced.

The ratio between the integral scale L_I and Kolmogorov scale η in the HIT used for the initial condition is 37, 79, 191, 373 and 664, ascending from the lowest to the highest Re_λ cases. Here, $L_I = (2k_T/3)^{3/2}/\varepsilon$ is evaluated with the turbulent kinetic energy (TKE) $k_T = \overline{u_i u_i}/2$ and its dissipation rate ε (Rosales & Meneveau 2005). The integral scale consistently exceeds the thickness of the shear layer, which is approximately 4η. The same DNS databases were used to explore the statistical properties of small-scale shear layers (Watanabe *et al.* 2020*b*). Notably, even at the smallest Re_λ value with $L_I/\eta = 37$, the characteristics of small-scale shear layers, when normalised by Kolmogorov scales, remain congruent with those observed at higher Re_λ (Watanabe *et al.* 2020*b*). A key parameter considered herein is the ratio of the perturbation wavelength λ_f to the Kolmogorov scale η. This study focuses on entrainment in shear-free turbulent fronts, chosen for their initial statistical homogeneity, which assures constant λ_f/η in the turbulent region at a fixed value of λ_f. In contrast, turbulent shear flows, such as jets and mixing layers, display statistical inhomogeneity, leading to spatial variations in λ_f/η. Previous studies indicate that mean shear effects exert minimal influence on the scaling of the TNTI and small-scale shear layers (Silva *et al.* 2018; Hayashi *et al.* 2021*b*), indicating that the findings from the shear-free turbulent front can be extended to more complex flows with mean shear.

The present DNS considers internal perturbations in the turbulent region. Both internal and external perturbations are applicable in laboratory experiments. Internal perturbations can be generated in turbulence by objects, such as cylinders and spheres in a mean flow, and settling particles, whose wakes produce velocity fluctuations at a certain scale (Britter *et al.* 1979; Nagata *et al.* 2020*b*; Kato *et al.* 2022). External perturbations can be introduced by fluidic actuators outside the turbulent region (Smith & Glezer 1998).

3. Entrainment analysis

The entrainment process is explored by examining the isosurface of vorticity magnitude ω at the outer edge of the turbulent front. As the vorticity decays over time with the evolution of the shear-free turbulent front, the normalised vorticity magnitude $\hat{\omega}$, defined as ω divided by the average $\overline{\omega}$ at $y = 0$, is utilized to identify the turbulent region. Similar normalisations are commonly employed to examine the TNTI in turbulent shear flows, where the mean vorticity magnitude decreases as the flow evolves (Bisset *et al.* 2002; Attili *et al.* 2014; Watanabe *et al.* 2018). Turbulent and non-turbulent regions are distinguishable by $\hat{\omega} > \omega_{th}$ and $\hat{\omega} \leqslant \omega_{th}$, respectively, using a threshold of ω_{th}. Given that ω rapidly diminishes to zero from the turbulent region across a thin TNTI layer, the identified turbulent region remains largely unaffected by the specific choice of ω_{th}, provided that ω_{th} is chosen from a range for which the detected turbulent volume does not depend on ω_{th}, as outlined in Taveira *et al.* (2013) and da Silva *et al.* (2014). This threshold insensitivity in the TNTI analysis has been documented for various flows (da Silva *et al.* 2014; Jahanbakhshi *et al.* 2015; Watanabe *et al.* 2018). The present investigation adopts $\omega_{th} = 0.01$, determined by assessing the ω_{th} dependence of the turbulent volume. Consequently, the surface bounding on the irrotational region, termed the irrotational boundary (Watanabe *et al.* 2015*b*; Zecchetto & da Silva 2021), is demarcated as an isosurface of $\hat{\omega} = \omega_{th}$. The irrotational boundary defines the outer edge of the TNTI layer, which has a finite thickness. Figure 1 also shows the irrotational boundary as an iso-vorticity line with $\hat{\omega} = 0.01$. The iso-vorticity line effectively separates the turbulent front characterised by large vorticity magnitude from the non-turbulent region with negligible vorticity.

The entrainment of the turbulent front is examined through analysis of the irrotational

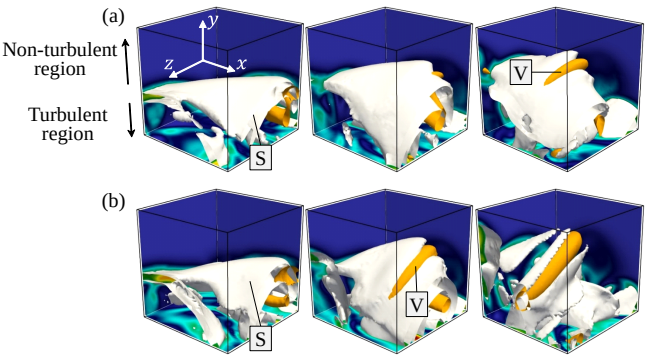

Figure 2: Temporal evolution of shear layers near the irrotational boundary for (*a*) R2 (unperturbed case) and (*b*) R2S14 (perturbed case). The isosurfaces of $I_R/\overline{I_R} = 6$ and $I_S/\overline{I_S} = 1.5$ represent vortices (orange) and shear layers (white), respectively. The mean intensities are evaluated at $y = 0$. From left to right, the time instances are $t/\tau_{\eta 0} = 2, 4$ and 6. The colour contour represents I_S.

boundary using isosurface area density, Σ', as described in Blakeley *et al.* (2022). The post-processing procedure is briefly outlined below, with a more in-depth exploration of Σ' available in Blakeley *et al.* (2022, 2023) and works referenced therein. In each snapshot, the detection function $X(x, y, z)$ of the turbulent region is defined such that $X = 1$ when $\hat{\omega}(x, y, z) \leqslant \omega_{th}$ and $X = 0$ when $\hat{\omega} > \omega_{th}$. The isosurface area density Σ' is then calculated as $\Sigma'(x, y, z) = -|\nabla\hat{\omega}|^{-1}\nabla X \cdot \nabla\hat{\omega}$. The isosurface area A is written as $A = \iiint_{\mathcal{V}} \Sigma' dxdydz$, where the integration spans the entire computational domain $\mathcal{V}$, while the volume of the turbulent region V_T is expressed using X as $V_T = \iiint_{\mathcal{V}}(1 - X)dxdydz$. The entrainment rate is defined as the temporal change in turbulent volume, represented by $\dot{V}_T = dV_T/dt$. The mean propagation velocity of the irrotational boundary is then evaluated as $V_P = \dot{V}_T/A$. These metrics related to entrainment may be compared between turbulent fronts originating from perturbed and unperturbed initial fields. For a given quantity Q, the relative disparity between the two cases, for example, R2S14 and R2, is evaluated as $\Delta Q = (Q_P - Q_U)/Q_U$, where Q_P and Q_U denote Q in the perturbed and unperturbed cases, respectively.

4. Results and discussion

The impact of perturbations on the turbulent front is first explored through visualisation of the shear layers. The triple decomposition of the velocity gradient tensor (Kolář 2007; Nagata *et al.* 2020*a*), is applied to obtain the local intensities of rigid-body rotation I_R and shearing motion I_S. Vortex tubes and shear layers can be identified using I_R and I_S, respectively. Figure 2(*a*) shows the temporal evolution of shear layers (white) and vortices (orange) near the irrotational boundary for R2, for which the initial field is derived from the original HIT without perturbations. Figure 2(*b*) shows the equivalent flow region and time range for R2S14, for which the perturbation wavelength corresponds to the unstable mode of small-scale shear instability. Both R2 and R2S14 initially observe the same shear layer, identified as 'S,' at $t/\tau_{\eta 0} = 2$. However, in the perturbed case, a vortex, designated as 'V,' forms within the shear layer by $t/\tau_{\eta 0} = 4$. Eventually, vortex formation occurs together with the breakdown of the shear layer at $t/\tau_{\eta 0} = 6$. In contrast, vortex formation occurs more gradually in the unperturbed case. Weak perturbations with $\lambda_f = 30\eta_0$ efficiently trigger shear instability at small scales near the TNTI layer, as previously observed for HIT (Watanabe & Nagata 2023).

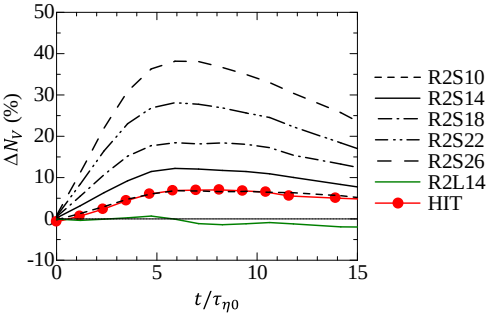

Figure 3: Changes in the number of vortices N_V by perturbations, represented by ΔN_V. HIT refers to the simulation of decaying homogeneous isotropic turbulence with a Reynolds number and perturbations corresponding to R2S10 (Watanabe & Nagata 2023).

In the case of HIT, the shear instability promoted by perturbations results in an increased number of vortices (Watanabe & Nagata 2023). This phenomenon is further confirmed for the shear-free turbulent front. Vortices are identified following the methodology presented in Jiménez *et al.* (1993) and Watanabe & Nagata (2023). Within this framework, the current study assumes that a grid point belongs to a vortex when the intensity of rigid-body rotation I_R normalised by its time-dependent average at $y = 0$, denoted by $\overline{I_R}$, surpasses a threshold I_{th}. Each separate region of vortex points constitutes a single vortex structure. Accordingly, the number of vortices, represented as N_V, is obtained as a function of time. Vortices are identified as regions with $I_R/\overline{I_R} > I_{th}$ with $I_{th} = 3$. Figure 3 presents the temporal variations of the relative difference between perturbed and unperturbed cases, ΔN_V, for the R2 series. Positive ΔN_V values signify an increase in vortices due to perturbation effects, negative values indicate a decrease and $\Delta N_V = 0$ suggests that perturbations do not influence the number of vortices. The plots of ΔN_V are therefore intended to examine the qualitative impacts of perturbations on vortices rather than to provide an exact number of vortices. Watanabe & Nagata (2023) evaluated the threshold (I_{th}) dependency of N_V, focusing on the perturbation response in HIT with the same methodology as in the present DNS. By plotting the number of vortices against I_{th}, they observed identical perturbation effects, namely an increase in N_V due to promoted shear instability, regardless of I_{th}. They also evaluated the potential of different variables to detect vortices, e.g. a second invariant of $\partial u_i/\partial x_j$, confirming that an increase in vortices is observed irrespective of the vortex identification method used. For the turbulent front in figure 3, perturbations initially have no influence on vortices, as shown by $\Delta N_V = 0$ at $t = 0$. When perturbations exhibit the optimal wavelength of shear instability (RnSa), an increase in ΔN_V is observed, suggesting that more vortices are generated when shear instability is promoted. No such increase is apparent in R2L14, where the perturbation wavelength considerably exceeds 30η. R2Sa cases with a representing a normalised amplitude demonstrate that perturbations with a larger amplitude have more pronounced effects on the number of vortices. The decaying HIT corresponding to R2S10 in Watanabe & Nagata (2023) may be compared with the shear-free turbulent front, showing that variations in ΔN_V are similar in both flows. The responses of small-scale shear layers to perturbations are consistent in both HIT and shear-free turbulent fronts. Watanabe & Nagata (2023) also demonstrated that the increment in vortices remains similar for different Reynolds numbers in HIT.

The ramifications of enhanced shear instability are explored for the entrainment rate, represented as $\dot{V}_T$. Figure 4(a) presents the temporal variations of the entrainment rate $\dot{V}_T$

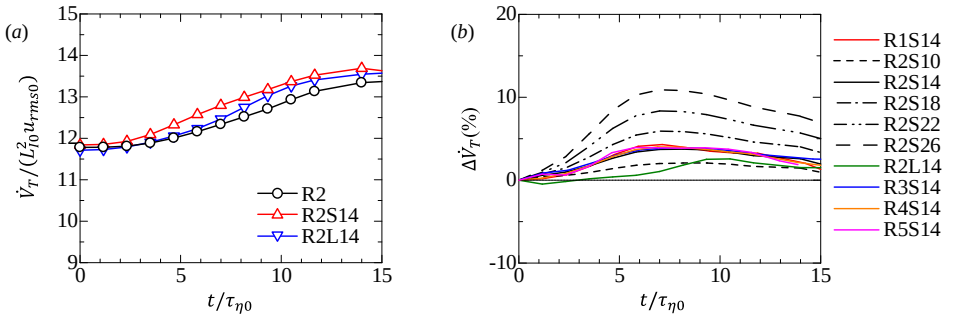

Figure 4: (*a*) Temporal variations of entrainment rate $\dot{V}_T$. (*b*) Changes due to perturbations in the entrainment rate $\dot{V}_T$, represented by $\Delta\dot{V}_T$.

for three cases. A positive value of $\dot{V}_T$ indicates the growth of the turbulent region. The entrainment rate is calculated using a second-order central difference on discrete data sets of $V_T(t)$. The entrainment rate in R2S14 becomes higher than in the other cases after $t/\tau_{\eta 0} \approx 2$. This amplified entrainment from $t/\tau_{\eta 0} \approx 2$ is virtually absent in R2L14 despite having the same perturbation amplitude as R2S14.

Figure 4(*b*) assesses the relative difference in the entrainment rate between perturbed and unperturbed cases by depicting $\Delta\dot{V}_T(t)$. Some simulation cases are omitted from the figure for clarity, although they are presented later to assess the Reynolds number dependence. Introducing perturbations that stimulate shear instability amplifies the entrainment rate, as shown by $\Delta\dot{V}_T > 0$ in the RnSa cases. Notably, $\Delta\dot{V}_T$ reaches its maximum at approximately $t/\tau_{\eta 0} \approx 7$ irrespective of the Reynolds number. The increase in vortices due to the shear instability promoted by perturbations is also most prominent at $t/\tau_{\eta 0} \approx 5$, as shown in figure 3. This consistency suggests that the activity of small-scale vortices plays a significant role in entrainment. After $t/\tau_{\eta 0} \approx 7$, $\Delta\dot{V}_T$ begins to decline and the influence of perturbations diminishes with time. When the perturbation wavelength is much larger than the unstable mode wavelength, the entrainment rate exhibits minimal change, as evidenced by the small $\Delta\dot{V}_T$ for R2L14. Consequently, the entrainment is enhanced when the perturbations are characterised by a wavelength similar in scale to the unstable mode of small-scale shear layers.

After imposing impulsive perturbations at a given time, the flow evolves freely. Although these perturbations initially cause an increase in the entrainment rate, indicated by $\Delta\dot{V}_T > 0$ in figure 4(*b*), a subsequent decrease of $\Delta\dot{V}_T$ occurs after reaching a peak, and the difference between the perturbed and unperturbed cases becomes small. This indicates that the perturbation effect is transient. Similarly, the impact on the number of vortices is also temporary, as evidenced by the analogous trend of ΔN_V in figure 3. Continuous or repetitive application of perturbations would more effectively sustain this enhanced entrainment. The transient enhancement of entrainment achieved by impulsive perturbations has important applications for chemically reacting flows. In situations where two reactants are introduced into separate flows, their mixing and subsequent reaction occur rapidly near the TNTI layer, especially when the reaction time scale is shorter than that of turbulence (Watanabe *et al.* 2013, 2014, 2015*a*; Jahanbakhshi & Madnia 2018; Ren *et al.* 2023). Thus, enhancing entrainment even for a short time could be leveraged to increase the reaction rate near the TNTI layer.

Entrainment is the process by which the non-turbulent fluid gains vorticity near the TNTI layer (Westerweel *et al.* 2005; Holzner & Lüthi 2011). A comparison of the enstrophy budget within the TNTI layer and around vortex tubes and shear layers suggests

that these small-scale structures are relevant to the entrainment process described by vorticity transport (Watanabe *et al.* 2017; Neamtu-Halic *et al.* 2021; Hayashi *et al.* 2021*b*). However, the mechanisms by which these structures locally cause entrainment has not yet been determined. A more straightforward way to understand entrainment is provided by Lagrangian viewpoints (Mathew & Basu 2002; Holzner & Lüthi 2011; Taveira *et al.* 2013; Watanabe *et al.* 2016*b*,*a*). Entrained fluid particles pass across the TNTI layers to reach the turbulent core region. The shear layers within the TNTI layer are unstable, and their roll-up generates vortex tubes as shown in figure 2. Layer roll-up causes a significant mixing of fluids on both sides of the shear layer (Winant & Browand 1974; Rogers & Moser 1992). One of the possible mechanisms by which small-scale structures cause entrainment is small-scale mixing associated with the roll-up of shear layers. The shear layers within the TNTI layer separate the turbulent and non-turbulent fluids (Elsinga & da Silva 2019; Hayashi *et al.* 2021*b*), which are expected to be mixed by shear instability. Another entrainment mechanism is directly related to the velocity distribution around vortex tubes and shear layers. Vortex tubes in turbulence form within an axial straining flow (Jiménez & Wray 1998; da Silva *et al.* 2011), which induces an inward flow to the vortex core (Davidson 2004). It has been noted that this inward velocity of vortex tubes can initiate entrainment (Watanabe *et al.* 2017) when the non-turbulent fluid is drawn into vortex tubes within the TNTI layer by the inward flow and is then further transferred into the turbulent core region by the rotating motion of the vortex. This explanation, based on the inward velocity of the straining flow, is also valid for shear layers within the TNTI layer because the shear layers undergo a biaxial strain with an inward velocity in the layer normal direction. The entrained fluid gains vorticity by viscous diffusion when it is transferred by the inward flow, and this entrainment process is consistent with Eulerian investigations of entrainment with vorticity transport.

The perturbation effect on the entrainment rate, described by $\Delta\dot{V}_T$, is similar to that of the number of vortices, ΔN_V. This correlation between $\Delta\dot{V}_T$ and ΔN_V has an important implication for the dominant entrainment mechanism. The perturbations promote shear instability, resulting in a greater number of vortices in the flow. The increase 'rate' of ΔN_V, $\partial\Delta N_V/\partial t$, provides a measure of the promotion of shear instability due to perturbations. As shown in figure 3, an increase in ΔN_V is observed for $t/\tau_\eta \leqslant 5$. The roll-up of shear layers in the perturbed cases is expected to occur more frequently than in the unperturbed cases for $t/\tau_\eta \leqslant 5$. If mixing due to the roll-up of shear layers dominates the entrainment process, $\Delta\dot{V}_T$ should be maximised until $t/\tau_\eta \leqslant 5$. However, this contradicts the results for $\Delta\dot{V}_T$ shown in figure 4(*b*). Instead, $\Delta\dot{V}_T$ and ΔN_V reach their peaks almost at the same time. This suggests that the entrainment rate is related to the number of vortices N_V rather than the increase rate of N_V due to perturbations. It should be noted that N_V is also correlated with the number of shear layers because the latter forms in the proximity of the former (Watanabe & Nagata 2023). Here, N_V concerns the vortices throughout the entire turbulent region; however, N_V can also be related to the number of vortices near the TNTI layer because vortices appear anywhere within the turbulent region. Indeed, the probability for vortex tubes and shear layers to appear at a given location does not change between the vicinity of the TNTI layer and the turbulent core region except within the viscous superlayer (da Silva *et al.* 2011; Hayashi *et al.* 2021*b*). The correlation between $\Delta\dot{V}_T$ and ΔN_V suggests that the presence of small-scale vortical structures near the TNTI layer plays an important role in entrainment, supporting a mechanism of entrainment linked to the inward flows of vortex tubes and shear layers as discussed above.

The entrainment rate is linked to two main factors: the surface area of the irrotational boundary A and the mean propagation velocity V_P. Figure 5 examines the perturbation-induced variations in A and V_P with ΔA and ΔV_P, respectively, both of which increase from

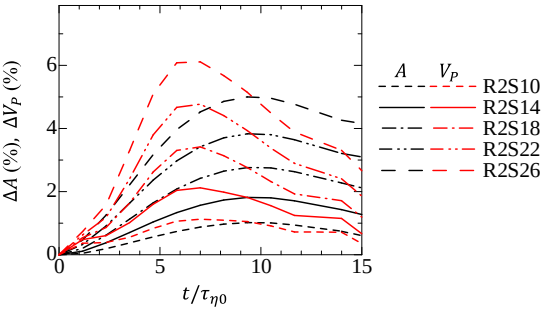

Figure 5: Changes due to perturbations in the isosurface area A and mean propagation velocity V_P, represented by ΔA and ΔV_P, respectively.

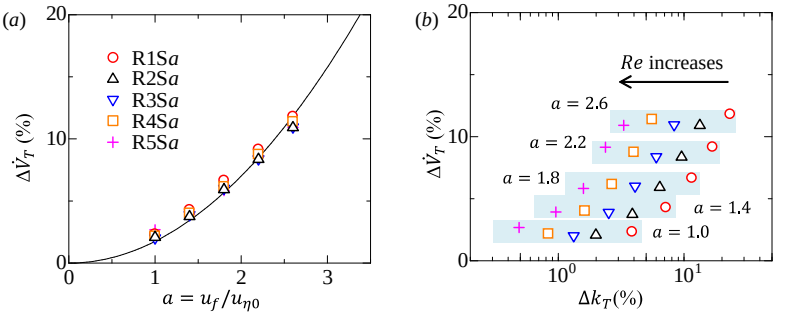

Figure 6: (a) Maximum values of the increase ratio of entrainment rate due to perturbations, represented by $\Delta\dot{V}_T$, plotted against the normalised perturbation amplitude $a = u_f/u_{\eta 0}$. (b) Maximum values of $\Delta\dot{V}_T$ plotted against the relative increase in turbulent kinetic energy due to the perturbations, represented by Δk_T.

0 with time. The combined effect of these increments culminates in an overall enhancement of the entrainment rate $\dot{V}_T = V_P A$. An increase in the area is expected from surface stretching due to vortices generated by shear instability (Neamtu-Halic *et al.* 2020).

Figure 6(a) shows the peak values of $\Delta\dot{V}_T$ in figure 4(b) plotted against the perturbation amplitude normalised by $u_{\eta 0}$ for all Reynolds number cases with $\Lambda = \mathrm{S}$ ($\lambda_f = 30\eta_0$). A larger amplitude results in greater enhancement of the entrainment. Notably, when normalised by the Kolmogorov velocity, the perturbation effects remain largely independent of the Reynolds numbers. $\Delta\dot{V}_T$ peaks approximately $7\tau_{\eta 0}$, which is also identical for all Reynolds numbers considered here. Thus, the enhancement of entrainment by small-scale shear instability occurs at the Kolmogorov scales.

The perturbations applied in the DNS presented herein result in an increase in the initial TKE, denoted as $k_T = \overline{u_i u_i}/2$. The relative increase is evaluated as $\Delta k_T = (k_{TP} - k_{T0})/k_{T0}$, wherein k_{TP} and k_{T0} correspond to the initial TKE at $y = 0$ for perturbed and unperturbed cases. Figure 6(b) displays the maximal $\Delta\dot{V}_T$ values for each case against Δk_T. The same entrainment enhancement can be achieved with weaker perturbations, i.e. smaller Δk_T, at a higher Reynolds number. An approximate 10% increase in the entrainment rate ($a = 2.2$) occurs with increases in the TKE of 2% and 12% for R5 and R1, respectively. The line in figure 6(a) illustrates an empirical fit using a quadratic function, represented by $\Delta\dot{V}_T = C_1 a^2$ with $C_1 = 1.7$, determined using a least squares method. This fitting function is introduced only for discussing the Reynolds number dependence for the range of a considered in this study and not for establishing the precise relationship between $\Delta\dot{V}_T$ and a. In fully developed

turbulent regions, a scaling of $u_{\eta 0}^2/k_{T0} \sim Re_\lambda^{-1}$ is anticipated (Pope 2000); hence, this empirical relation for $\Delta\dot{V}_T$ suggests a scaling of $\Delta\dot{V}_T \sim (u_f^2/k_{T0})Re_\lambda$. For the present test case, the energy introduced by the perturbation required to achieve equivalent entrainment enhancement ($\Delta\dot{V}_T$) decreases as Re_λ^{-1} with increasing Reynolds numbers. R2L14 investigates the influence of perturbations with a wavelength significantly larger than the unstable mode wavelength of shear layers. Under such conditions, perturbations exert minimal influence on small-scale vortices and entrainment rate, as shown in figures 3 and 4(*b*). A weak influence of large-scale perturbations was also reported for vortices in HIT (Watanabe & Nagata 2023). The perturbations in R2L14 lead to an increase in the initial kinetic energy by $\Delta k_T = 1.3\%$. This increment is similar to that in R5S18, where $\Delta k_T = 1.5\%$. For R5S18, the entrainment rate increases by approximately 6%. In the numerical setup used for this study, the original HIT exhibits a turbulent kinetic energy of approximately $k_{T0} \approx 1.5$ (arbitrary units), irrespective of the Reynolds number. Therefore, the similarity between the Δk_T values in these two cases indicates that their initial kinetic energies are also comparable. However, the influence of perturbations is evident only when the wavelength aligns with the unstable mode of shear layers. This comparison suggests that the kinetic energy added by perturbations alone is not a significant factor in enhancing entrainment; rather, the wavelength of the perturbations plays a crucial role. Additionally, no clear correlation is observed between the entrainment rate and Δk_T across different Reynolds numbers in figure 6(*b*). The kinetic energy increment alone does not dictate the enhancement in entrainment rate. Instead, the perturbation amplitude (analogous to the kinetic energy of perturbations) normalised by the Kolmogorov velocity determines the increase in entrainment rate. This may be related to the scaling of shear layers. The velocity jump across the shear layers is also determined by the Kolmogorov velocity (Watanabe *et al.* 2020*b*; Hayashi *et al.* 2021*a*; Fiscaletti *et al.* 2021).

5. Conclusions

The numerical experiments reported in this study demonstrate that entrainment rate can be significantly amplified by introducing perturbations with wavelengths corresponding to the unstable mode of small-scale shear layers, i.e., at approximately 30 times the Kolmogorov scale. These perturbations efficiently stimulate the shear layers near the TNTI layer and accelerate vortex formations due to instability. The effects of impulsive perturbations on entrainment and vortices are transient, diminishing over time. The Kolmogorov scales primarily govern the process underlying the entrainment enhancement. Even weak perturbations can yield substantial enhancements in entrainment via small-scale shear instability, especially at higher Reynolds numbers, due to the smaller value of the corresponding Kolmogorov velocity. The statistical behaviour of small-scale shear layers are minimally influenced by flow types (Elsinga & Marusic 2010; Watanabe *et al.* 2020*b*; Hayashi *et al.* 2021*a*; Fiscaletti *et al.* 2021), suggesting that this method of enhancement is applicable to various turbulent flows. Furthermore, turbulent flows are filled with many small-scale shear layers, which exist anywhere in turbulent regions (Horiuti & Takagi 2005; Pirozzoli *et al.* 2010; Buxton & Ganapathisubramani 2010; Nagata *et al.* 2020*a*; Hayashi *et al.* 2021*a*; Fiscaletti *et al.* 2021). Intricate sensing mechanisms are not required to locate and manipulate these shear layers, unlike other active flow control techniques that rely on identifying specific turbulent structures. Although the results reported herein are derived from idealised numerical experiments conducted under controlled conditions, the resulting features of small-scale shear instability have broad practical applications, from engineering to environmental flows. Although additional research, including experimental validation, is required for future applications, the present study introduces a new and widely

applicable framework for flow control that leverages small-scale shear instabilities triggered by weak and small-scale disturbances.

Acknowledgements. Numerical simulations presented in this paper were performed using the high-performance computing systems at the Japan Agency for Marine-Earth Science and Technology and Nagoya University. This work was also supported by a Collaborative Research Project on Computer Science with High-Performance Computing in Nagoya University.

Funding. This work was supported by JSPS KAKENHI Grant Number JP22K03903.

Declaration of interests. The authors report no conflicts of interest.

Data availability statement. The data supporting the findings of this study are available from the corresponding author upon reasonable request.

Appendix A. Effects of the initial transition of a shear-free turbulent front on entrainment enhancement

DNS of the shear-free turbulent front conducted in this study was initialised using a velocity field featuring an artificial interface generated by a truncated velocity field defined by (2.1). The flow evolution at an early time is influenced by the initial conditions, which may affect the observed entrainment enhancement. This appendix addresses the dependence of entrainment enhancement on the time at which perturbations are imposed. To this end, DNS is performed for two additional cases involving the transfer of a passive scalar ϕ, whose evolution is governed by an advection-diffusion equation (Watanabe *et al.* 2015*b*). The Schmidt number, $Sc = \nu/D$, is set to 1, where D represents the diffusivity coefficient. The initial distribution of the passive scalar ϕ is specified as $\phi(y) = C(y)$, which is one in the turbulent region and zero in the non-turbulent region. The passive scalar with $Sc = 1$ serves as the marker of the turbulent region. The interfaces identified using vorticity and passive scalar are consistent, exhibiting minimal differences in both the location and the local curvature of the isosurfaces (Gampert *et al.* 2014; Watanabe *et al.* 2018). Perturbations are introduced into the turbulent core region with $\phi > 0.5$ after the flow has evolved from the initial condition for a time T. The Kolmogorov scales corresponding to the time at which the perturbations are added are denoted by η_P, $\tau_{\eta P}$ and $u_{\eta P}$. These scales are evaluated by considering a volume average of the energy dissipation rate in the turbulent region identified with the vorticity magnitude. The simulations in this appendix are conducted for R2, $\lambda_f = 30\eta_P$ and $u_f = 1.4u_{\eta P}$. Based on the integral time scale $\tau_I = L_I/\sqrt{2k_T/3}$ defined using the turbulent kinetic energy k_T and the characteristic length scale of large-scale motions L_I, T is determined to be either 0 or $0.51\tau_I$ ($9.4\tau_\eta$). Here, τ_I and τ_η are evaluated for the original HIT used for the initial conditions of the shear-free turbulent front. Figure 7 visualises the shear-free turbulent front at $t = 9.4\tau_\eta$. The flow evolves until this time instance, and then the sinusoidal perturbations described in § 2 are introduced into the region with $\phi > 0.5$. In this appendix, the results of a single simulation for each case are presented without taking ensemble averages of different simulations.

Figure 8(a) plots the entrainment rate $\dot{V}_T$ as a function of $t - T$, which represents the time after adding the perturbation. The results are compared between the perturbed and unperturbed cases. Regardless of the time T at which the perturbations are added, the perturbed cases exhibit larger $\dot{V}_T$ values than the corresponding unperturbed cases. The choice of T influences the temporal evolution of $\dot{V}_T$ because of the transient behaviour of the shear-free turbulent front at early times. Figure 8(b) illustrates changes in entrainment rate due to perturbations, denoted as $\Delta\dot{V}_T$. The temporal variation of $\Delta\dot{V}_T$ is quantitatively similar for all cases. Entrainment enhancement is observed for both T values, and is not influenced by the initial transient behaviour of the shear-free turbulent front.

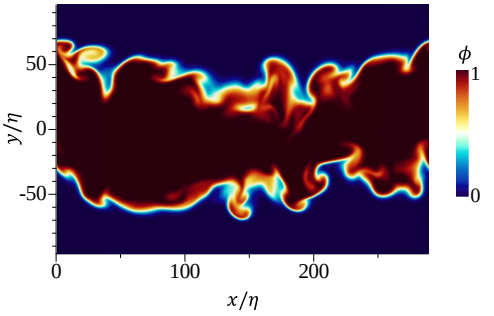

Figure 7: The shear-free turbulent front visualised by passive scalar ϕ at $t = 9.4\tau_\eta$ in R2. The coordinates are normalised by the Kolmogorov scale η at $y = 0$.

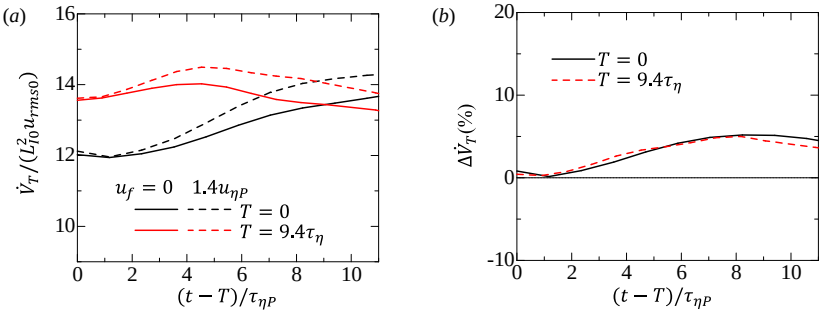

Figure 8: (a) Entrainment rate $\dot{V}_T$ plotted as a function of time after adding perturbations, $t - T$. The results are compared between the perturbed ($u_f = 1.4u_{\eta P}$) and unperturbed ($u_f = 0$) cases. (b) Changes due to perturbations in the entrainment rate, represented by $\Delta\dot{V}_T$.

REFERENCES

Attili, A., Cristancho, J. C. & Bisetti, F. 2014 Statistics of the turbulent/non-turbulent interface in a spatially developing mixing layer. *J. Turbulence* **15** (9), 555–568.

Betchov, R. & Szewczyk, A. 1963 Stability of a shear layer between parallel streams. *Phys. Fluids* **6** (10), 1391–1396.

Bisset, D. K., Hunt, J. C. R. & Rogers, M. M. 2002 The turbulent/non-turbulent interface bounding a far wake. *J. Fluid Mech.* **451**, 383–410.

Blakeley, B. C., Olson, B. J. & Riley, J. J. 2022 Self-similarity of scalar isosurface area density in a temporal mixing layer. *J. Fluid Mech.* **951**, A44.

Blakeley, B. C., Olson, B. J. & Riley, J. J. 2023 On the evolution of scalar iso-surface area density in a turbulent mixing layer. *J. Fluid Mech.* **966**, A33.

Britter, R. E., Hunt, J. C. R. & Mumford, J. C. 1979 The distortion of turbulence by a circular cylinder. *J. Fluid Mech.* **92** (2), 269–301.

Buxton, O. R. H. & Ganapathisubramani, B. 2010 Amplification of enstrophy in the far field of an axisymmetric turbulent jet. *J. Fluid Mech.* **651**, 483–502.

Cattafesta III, L. N. & Sheplak, M. 2011 Actuators for active flow control. *Annu. Rev. Fluid Mech.* **43**, 247–272.

Cimarelli, A., Cocconi, G., Frohnapfel, B. & De Angelis, E. 2015 Spectral enstrophy budget in a shear-less flow with turbulent/non-turbulent interface. *Phys. Fluids* **27** (12).

Davidson, P. A. 2004 *Turbulence: An Introduction for Scientists and Engineers*. Oxford Univ. Pr.

Eisma, J., Westerweel, J., Ooms, G. & Elsinga, G. E. 2015 Interfaces and internal layers in a turbulent boundary layer. *Phys. Fluids* **27** (5), 055103.

Elsinga, G. E. & Marusic, I. 2010 Universal aspects of small-scale motions in turbulence. *J. Fluid Mech.* **662**, 514–539.

Elsinga, G. E. & da Silva, C. B. 2019 How the turbulent/non-turbulent interface is different from internal turbulence. *J. Fluid Mech.* **866**, 216–238.

Enoki, R., Watanabe, T. & Nagata, K. 2023 Statistical properties of shear and nonshear velocity components in isotropic turbulence and turbulent jets. *Phys. Rev. Fluids* **8** (10), 104602.

Fiscaletti, D., Buxton, O. R. H. & Attili, A. 2021 Internal layers in turbulent free-shear flows. *Phys. Rev. Fluids* **6** (3), 034612.

Gampert, M., Boschung, J., Hennig, F., Gauding, M. & Peters, N. 2014 The vorticity versus the scalar criterion for the detection of the turbulent/non-turbulent interface. *J. Fluid Mech.* **750**, 578–596.

Gul, M., Elsinga, G. E. & Westerweel, J. 2020 Internal shear layers and edges of uniform momentum zones in a turbulent pipe flow. *J. Fluid Mech.* **901**, A10.

Hayashi, M., Watanabe, T. & Nagata, K. 2021*a* Characteristics of small-scale shear layers in a temporally evolving turbulent planar jet. *J. Fluid Mech.* **920**, A38.

Hayashi, M., Watanabe, T. & Nagata, K. 2021*b* The relation between shearing motions and the turbulent/non-turbulent interface in a turbulent planar jet. *Phys. Fluids* **33** (5), 055126.

Holzner, M. & Lüthi, B. 2011 Laminar superlayer at the turbulence boundary. *Phys. Rev. Lett.* **106** (13), 134503.

Horiuti, K. & Takagi, Y. 2005 Identification method for vortex sheet structures in turbulent flows. *Phys. Fluids* **17** (12), 121703.

Jahanbakhshi, R. & Madnia, C. K. 2016 Entrainment in a compressible turbulent shear layer. *J. Fluid Mech.* **797**, 564–603.

Jahanbakhshi, R. & Madnia, C. K. 2018 The effect of heat release on the entrainment in a turbulent mixing layer. *J. Fluid Mech.* **844**, 92–126.

Jahanbakhshi, R., Vaghefi, N. S. & Madnia, C. K. 2015 Baroclinic vorticity generation near the turbulent/non-turbulent interface in a compressible shear layer. *Phys. Fluids* **27** (10), 105105.

Jiménez, J. & Wray, A. A. 1998 On the characteristics of vortex filaments in isotropic turbulence. *J. Fluid Mech.* **373**, 255–285.

Jiménez, J., Wray, A. A., Saffman, P. G. & Rogallo, R. S. 1993 The structure of intense vorticity in isotropic turbulence. *J. Fluid Mech.* **255**, 65–90.

Kato, H., Takamure, K. & Uchiyama, T. 2022 Characteristics of vortex shedding in the wake of a sphere with a uniaxial through-hole. *AIP Adv.* **12** (10).

Kolář, V. 2007 Vortex identification: New requirements and limitations. *Int. J. Heat Fluid Flow* **28** (4), 638–652.

Kolář, V. & Šístek, J. 2014 Recent progress in explicit shear-eliminating vortex identification. In *Proceedings of the 19th Australasian Fluid Mechanics Conference*.

Krug, D., Holzner, M., Lüthi, B., Wolf, M., Kinzelbach, W. & Tsinober, A. 2015 The turbulent/non-turbulent interface in an inclined dense gravity current. *J. Fluid Mech.* **765**, 303–324.

Krug, D., Holzner, M., Marusic, I. & van Reeuwijk, M. 2017 Fractal scaling of the turbulence interface in gravity currents. *J. Fluid Mech.* **820**.

Lin, S. J. & Corcos, G. M. 1984 The mixing layer: deterministic models of a turbulent flow. Part 3. The effect of plane strain on the dynamics of streamwise vortices. *J. Fluid Mech.* **141**, 139–178.

Mahrt, L. 1999 Stratified atmospheric boundary layers. *Boundary-Layer Meteorol.* **90** (3), 375–396.

Mathew, J. & Basu, A. J. 2002 Some characteristics of entrainment at a cylindrical turbulence boundary. *Phys. Fluids* **14** (7), 2065–2072.

Mellado, J. P. 2017 Cloud-top entrainment in stratocumulus clouds. *Annu. Rev. Fluid Mech.* **49**, 145–169.

Mistry, D., Philip, J., Dawson, J. R. & Marusic, I. 2016 Entrainment at multi-scales across the turbulent/non-turbulent interface in an axisymmetric jet. *J. Fluid Mech.* **802**, 690–725.

Morinishi, Y., Lund, T. S., Vasilyev, O. V. & Moin, P. 1998 Fully conservative higher order finite difference schemes for incompressible flow. *J. Comput. Phys.* **143** (1), 90–124.

Nagata, R., Watanabe, T., Nagata, K. & da Silva, C. B. 2020*a* Triple decomposition of velocity gradient tensor in homogeneous isotropic turbulence. *Comput. Fluids* **198**, 104389.

Nagata, T., Noguchi, A., Kusama, K., Nonomura, T., Komuro, A., Ando, A. & Asai, K. 2020*b* Experimental investigation on compressible flow over a circular cylinder at Reynolds number of between 1000 and 5000. *J. Fluid Mech.* **893**, A13.

Neamtu-Halic, M. M., Krug, D., Mollicone, J.-P., van Reeuwijk, M., Haller, G. & Holzner, M. 2020 Connecting the time evolution of the turbulence interface to coherent structures. *J. Fluid Mech.* **898**.

Neamtu-Halic, M. M., Mollicone, J.-P., Van Reeuwijk, M. & Holzner, M. 2021 Role of vortical structures for enstrophy and scalar transport in flows with and without stable stratification. *J. Turbul.* **22** (7), 393–412.

Pirozzoli, S., Bernardini, M. & Grasso, F. 2010 On the dynamical relevance of coherent vortical structures in turbulent boundary layers. *J. Fluid Mech.* **648**, 325–349.

Pope, S. B. 2000 *Turbulent Flows*. Cambridge Univ. Pr.

van Reeuwijk, M. & Holzner, M. 2014 The turbulence boundary of a temporal jet. *J. Fluid Mech.* **739**, 254–275.

Ren, J., Wang, H., Luo, K. & Fan, J. 2023 Investigation of entrainment and its effect on flame stabilization in a turbulent high Karlovitz number premixed jet flame using direct numerical simulation. *Flow, Turbul. Combust.* pp. 1–20.

Rogers, M. M. & Moser, R. D. 1992 The three-dimensional evolution of a plane mixing layer: the Kelvin–Helmholtz rollup. *J. Fluid Mech.* **243**, 183–226.

Rosales, C. & Meneveau, C. 2005 Linear forcing in numerical simulations of isotropic turbulence: Physical space implementations and convergence properties. *Phys. Fluids* **17** (9), 095106.

Sardina, G., Picano, F., Brandt, L. & Caballero, R. 2015 Continuous growth of droplet size variance due to condensation in turbulent clouds. *Phys. Rev. Lett.* **115** (18), 184501.

Schols, J. L. J. 1984 The detection and measurement of turbulent structures in the atmospheric surface layer. *Bound.-Layer Meteor.* **29**, 39–58.

da Silva, C. B., Dos Reis, R. J. N. & Pereira, J. C. F. 2011 The intense vorticity structures near the turbulent/non-turbulent interface in a jet. *J. Fluid Mech.* **685**, 165–190.

da Silva, C. B., Hunt, J. C. R., Eames, I. & Westerweel, J. 2014 Interfacial layers between regions of different turbulence intensity. *Annu. Rev. Fluid Mech.* **46**, 567–590.

Silva, T. S., Zecchetto, M. & da Silva, C. B. 2018 The scaling of the turbulent/non-turbulent interface at high Reynolds numbers. *J. Fluid Mech.* **843**, 156.

Smith, B. L. & Glezer, A. 1998 The formation and evolution of synthetic jets. *Phys. Fluids* **10** (9), 2281–2297.

Taveira, R. R., Diogo, J. S., Lopes, D. C. & da Silva, C. B. 2013 Lagrangian statistics across the turbulent-nonturbulent interface in a turbulent plane jet. *Phys. Rev. E* **88** (4), 043001.

Taveira, R. R. & da Silva, C. B. 2014 Characteristics of the viscous superlayer in shear free turbulence and in planar turbulent jets. *Phys. Fluids* **26** (2), 021702.

Vincent, A. & Meneguzzi, M. 1994 The dynamics of vorticity tubes in homogeneous turbulence. *J. Fluid Mech.* **258**, 245–254.

Watanabe, T., Jaulino, R., Taveira, R. R., da Silva, C. B., Nagata, K. & Sakai, Y. 2017 Role of an isolated eddy near the turbulent/non-turbulent interface layer. *Phys. Rev. Fluids* **2** (9), 094607.

Watanabe, T. & Nagata, K. 2023 The response of small-scale shear layers to perturbations in turbulence. *J. Fluid Mech.* **963**, A31.

Watanabe, T., Naito, T., Sakai, Y., Nagata, K. & Ito, Y. 2015*a* Mixing and chemical reaction at high schmidt number near turbulent/nonturbulent interface in planar liquid jet. *Phys. Fluids* **27** (3), 035114.

Watanabe, T., Sakai, Y., Nagata, K., Ito, Y. & Hayase, T. 2014 Reactive scalar field near the turbulent/non-turbulent interface in a planar jet with a second-order chemical reaction. *Phys. Fluids* **26** (10), 105111.

Watanabe, T., Sakai, Y., Nagata, K., Ito, Y. & Hayase, T. 2015*b* Turbulent mixing of passive scalar near turbulent and non-turbulent interface in mixing layers. *Phys. Fluids* **27** (8), 085109.

Watanabe, T., Sakai, Y., Nagata, K., Terashima, O., Suzuki, H., Hayase, T. & Ito, Y. 2013 Visualization of turbulent reactive jet by using direct numerical simulation. *Int. J. Model. Simul. Sci. Comput.* **4**, 1341001.

Watanabe, T., da Silva, C. B. & Nagata, K. 2016*a* Multi-particle dispersion during entrainment in turbulent free-shear flows. *J. Fluid Mech.* **805**, R1.

Watanabe, T., da Silva, C. B. & Nagata, K. 2020*a* Scale-by-scale kinetic energy budget near the turbulent/nonturbulent interface. *Phys. Rev. Fluids* **5** (12), 124610.

Watanabe, T., da Silva, C. B., Sakai, Y., Nagata, K. & Hayase, T. 2016*b* Lagrangian properties of the entrainment across turbulent/non-turbulent interface layers. *Phys. Fluids* **28** (3), 031701.

Watanabe, T., Tanaka, K. & Nagata, K. 2020*b* Characteristics of shearing motions in incompressible isotropic turbulence. *Phys. Rev. Fluids* **5** (7), 072601(R).

Watanabe, T., Zhang, X. & Nagata, K. 2018 Turbulent/non-turbulent interfaces detected in DNS of incompressible turbulent boundary layers. *Phys. Fluids* **30** (3), 035102.

612 Westerweel, J., Fukushima, C., Pedersen, J. M. & Hunt, J. C. R. 2005 Mechanics of the turbulent-
613 nonturbulent interface of a jet. *Phys. Rev. Lett.* **95** (17), 174501.
614 Westerweel, J., Fukushima, C., Pedersen, J. M. & Hunt, J. C. R. 2009 Momentum and scalar transport
615 at the turbulent/non-turbulent interface of a jet. *J. Fluid Mech.* **631**, 199–230.
616 Winant, C. D. & Browand, F. K. 1974 Vortex pairing: the mechanism of turbulent mixing-layer growth at
617 moderate Reynolds number. *J. Fluid Mech.* **63** (2), 237–255.
618 Zecchetto, M. & da Silva, C. B. 2021 Universality of small-scale motions within the turbulent/non-
619 turbulent interface layer. *J. Fluid Mech.* **916**, A9.